Vibrational deactivation of $N_2(v=1)$ by inelastic collisions with ^3He and ^4He: An experimental and a theoretical study

J. P. Reid
Physical Chemistry Laboratory, South Parks Road, Oxford OX1-3QZ, United Kingdom

A. J. Thakkar
Department of Chemistry, University of New Brunswick, Fredericton, New Brunswick E3B 6E2, Canada

P. W. Barnes
Physical Chemistry Laboratory, South Parks Road, Oxford OX1 3QZ, United Kingdom

E. F. Archibong
Department of Chemistry, Jackson State University, Jackson, Mississippi 39217

H. M. Quiney
Department of Physics, Clarendon Laboratory, Parks Road, Oxford OX1 3PU, United Kingdom

C. J. S. M. Simpson
Physical Chemistry Laboratory, South Parks Road, Oxford OX1-3QZ, United Kingdom

(Received 15 April 1997; accepted 13 May 1997)

A new N_2–He intermolecular potential with vibrational coordinate dependence is presented. Rate constants for the vibrational deactivation of $N_2(v=1)$ by He in the gas phase have been calculated over the temperature range 5–300 K. Accurate values of the rate constants for this process are known down to 100 K. We have now extended these measurements down to 70 K for the deactivation of $^{14}N_2(v=1)$ by ^{4}He and down to 50 K for the deactivation of $^{15}N_2(v=1)$ by ^{3}He. Agreement between the theoretically calculated and the experimentally determined rate constants is excellent with the calculated values reproducing the experimental measurements within their error bars. An investigation of the low impact energy regime is also presented. While this focuses on collision energies of less than $20\ cm^{-1}$ and yields rate constants which are in a temperature region inaccessible to our experimental method, it gives further insights into the influence of the attractive well on vibrational energy transfer processes. © *1997 American Institute of Physics.* [S0021-9606(97)04031-2]

I. INTRODUCTION

Experimental and theoretical studies of the vibrational relaxation of $CO(v=1)$ by light mass collision partners have shown that, at temperatures below the Lennard-Jones well depth, attractive forces influence the collisional deactivation processes. The experimentally determined rate constants for the deactivation of $CO(v=1)$ by the isotopomers of hydrogen[1,2] show an upturn in their values below 60 K, the Lennard-Jones well depth for these systems being 64 K.[3] While no upturn has been observed experimentally in the rate constants for the deactivation of $CO(v=1)$ by helium,[1,2] an upturn has been shown to occur from theoretical calculations at temperatures lower than 35 K (Ref. 4) which is the lowest temperature currently accessible to our experiments. The upturn has been attributed to the occurrence of orbiting resonances at low impact energies. A theoretical study of the deactivation of $CO(v=1)$ by hydrogen has shown that the deeper attractive well for this system influences the collisional process at much higher impact energies than in the CO–He system.[5] It is essential to consider not only the importance of the well depth in determining the behavior of the relaxation rate constants at low temperatures,[6,7] but also the influence of the anisotropy of the interaction well and the part it plays in enabling the formation of orbiting resonances at higher impact energies and higher orbital angular momenta. A previous theoretical study on the He–N_2 potential energy surface calculated by Banks *et al.*, hereafter denoted the CEPA (coupled electron pair approximation) surface,[8] although providing a convenient starting point, revealed major deficiencies in the interaction surface especially in the low kinetic energy region with which we are interested.[9]

A recent paper by Hu and Thakkar presented a new He–N_2 interaction surface[10] which is calculated at one fixed N_2 bond length and is hence only vibrationally elastic. This potential is thought to have the necessary anisotropy suggested by beam experiments.[11] It reproduces the experimental second virial coefficients reasonably well and the authors conclude that the surface is ''unlikely to differ from the true potential energy surface (PES) by more than 10% over the range of intermolecular distances ($4a_0-10a_0$) sampled'' in their work. They conclude by inviting further work to test their assertion.

Vibrational energy transfer provides a stringent test of any intermolecular potential energy surface. To calculate accurate thermally averaged rate constants, scattering calculations must be performed at a large number of impact energies which sample both the high repulsive wall of a surface and also, in the low temperature regime, the low repulsive wall, and attractive well regions. In order to further test the accuracy of this new N_2–He surface, the calculation of vibrational energy transfer rate constants was undertaken. It is important to note that the collision cross sections which are

calculated are extremely small and so are the thermally averaged rate constants. These calculations are therefore not only a stringent test of the intermolecular potential but are also a demanding test of the numerical procedures and methods adopted.

The original surface was calculated at one fixed N_2 bond length. For the study of vibrational relaxation it is necessary to know the dependence of the interaction energy on the vibrational coordinate of the vibrationally excited diatom. The original fourth order, Møller–Plesset perturbation calculations have been extended to include the vibrational coordinate dependence. This extension of the surface is presented in Sec. III with the scattering calculations presented in Sec. IV. In order to consider the accuracy of the low repulsive wall region of the interaction surface we have extended the experimentally measured rate constants from 100 K down to the lowest experimentally accessible temperature of 70 K for the $^{14}N_2$–^{4}He system and 50 K for the $^{15}N_2$–^{3}He system. The experimental study and the results obtained are presented in Sec. II. Finally, in Sec. V, we compare the theoretically calculated and experimentally determined values of the relaxation rate constants.

II. EXPERIMENT

A. Apparatus

The apparatus used for the present study has been described in detail in previous publications[1,12] and only a brief description will be given here. Experiments are performed in a fluorescence cell which is housed in an Oxford Instruments cryostat. The cell may be cooled with liquid N_2 or with liquid He and the temperature of the cell can be stabilized to ± 0.1 K within the temperature range 15–300 K. A liquid nitrogen cooled InSb detector is mounted in the perpendicular vertical plane to the incident frequency doubled radiation from a CO_2 laser. Fluorescence traces are collected by a Datalab DL912 transient recorder and analyzed by custom written computer software.[13] The frequency doubled $9R(18)$ line of the regular band of the CO_2 laser is within 0.007 cm^{-1} of the $R(2)$ line of $^{12}C^{16}O$. Pumping such a low J transition enables us to reach temperatures as low as 35 K,[1] below which the vapor pressure of CO falls rapidly and the signal-to-noise ratio becomes too small to allow experimental measurements to be made. The output of the CO_2 laser is frequency doubled by means of a $AgGaSe_2$ crystal with the undoubled radiation attenuated by means of two ZnSe Brewster angle windows to give pulse energies in the range 0.5–2 mJ. The purities of the gases used are given in Table I.

TABLE I. Gas purity levels.

Gas	% Purity	Principal impurities
$^{12}C^{16}O$	^{12}C 99.999 at. %	(N_2 0.1, (CO_2 0.1, O_2 0.1) %
$^{14}N_2$	99.9995	(O_2<2, H_2<1, hydrocarbons<0.1, CO/CO_2<0.5, H_2O<1) ppm
$^{15}N_2$	^{15}N 99 at. %	(H_2O 0.12, (O_2 0.04, Ar 0.03) %
^{4}He	99.999	(N_2 5, (O_2 2, H_2 1, CO_2 0.5, hydrocarbons 0.5, H_2O 1) ppm
^{3}He	99.99	Not stated

B. System analysis

In these experiments we used CO as a collisional pump for either $^{14}N_2$ or $^{15}N_2$:

$$^{12}C^{16}O(v=1)+{}^{14}N_2(v=0) \rightleftharpoons {}^{12}C^{16}O(v=0)+{}^{14}N_2(v=1)+(\Delta\overline{\nu}=-188\ cm^{-1}), \quad (1)$$

$$^{12}C^{16}O(v=1)+{}^{15}N_2(v=0) \rightleftharpoons {}^{12}C^{16}O(v=0)+{}^{15}N_2(v=1)+(\Delta\overline{\nu}=-108\ cm^{-1}). \quad (2)$$

The coupling rate for the formation of the CO/N_2 coupled pair is given by Eq. (3). k_f is the rate constant for the forward endothermic transfer and k_b is the rate constant for the backward transfer from $N_2(v=1)$ into $CO(v=1)$:[14–16]

$$\lambda_c=(k_f\chi_{N_2}+k_b\chi_{CO})p_T. \quad (3)$$

The mole fractions of CO and N_2 are denoted by χ_{CO} and χ_{N_2}, respectively, and the total pressure at which the experiment is performed is denoted by p_T. Conditions are selected so that the transfer is rapid in comparison to the rate of the deactivation process which is being measured: it is typically faster by between 1 and 2 orders of magnitude. It is also necessary to ensure that a small fraction of the energy remains in the CO molecule once the coupling equilibration is complete in order that the relaxation processes occurring can be monitored. The remainder of the kinetic scheme is given below.

$$^{12}C^{16}O(v=1)+He \rightarrow {}^{12}C^{16}O(v=0)+He+(\Delta\overline{\nu}=2143\ cm^{-1}), \quad (4)$$

$$^{14}N_2(v=1)+He \rightarrow {}^{14}N_2(v=0)+He+(\Delta\overline{\nu}=2330\ cm^{-1}), \quad (5)$$

$$^{15}N_2(v=1)+He \rightarrow {}^{15}N_2(v=0)+He+(\Delta\overline{\nu}=2250\ cm^{-1}), \quad (6)$$

$$^{12}C^{16}O(v=1) \rightarrow {}^{12}C^{16}O(v=0)+h\nu(=2143\ cm^{-1}). \quad (7)$$

The rates of vibrational deactivation of both $CO(v=1)$ and N_2 by CO and N_2 are far too slow to contribute to the observed decay. In the limiting conditions in which the rate of the formation of the coupled pair and the rates of deactivation processes (4)–(7) are well separated in their timescales, the observed fluorescence decay of $CO(v=1)$ can be viewed as the combination of a fast decaying exponential, λ_c, and a slower decaying exponential, λ_s. If we look at the slower decaying portion, its characteristic rate of decay can be approximated as

$$\lambda_s=f_{CO}k_{CO-He}\chi_{He}p_T+f_{N_2}k_{N_2-He}\chi_{He}p_T+f_{CO}k_{rad}+\rho_{imp}. \quad (8)$$

TABLE II. The $^{14}N_2$–^{4}He and $^{15}N_2$–^{3}He systems: Experimental rate constants (in units of cm^3 mol^{-1} s^{-1}).

Temperature (K)	$k_{^{14}N_2-^4He}$	Temperature (K)	$k_{^{15}N_2-^3He}$
70	$(1.8\pm0.2)(-20)$[a]	50	$(2.3\pm0.4)(-19)$[d]
75	$(2.3\pm0.3)(-20)$[b]	55	$(2.5\pm0.2)(-19)$[d]
80	$(2.6\pm0.2)(-20)$[a]	60	$(2.7\pm0.1)(-19)$[d]
85	$(3.3\pm0.2)(-20)$[b]	70	$(3.5\pm0.1)(-19)$[d]
90	$(3.8\pm0.2)(-20)$[a]	80	$(4.7\pm0.3)(-19)$[d]
100	$(5.4\pm0.1)(-20)$[a]	90	$(6.3\pm0.2)(-19)$[d]
100	$(5.2\pm0.3)(-20)$[b]	100	$(7.8\pm0.4)(-19)$[d]
100	$(5.5\pm0.3)(-20)$[c]	120	$(1.3\pm0.1)(-18)$[d]
150	$(2.3\pm0.2)(-19)$[c]		
200	$(9.1\pm0.6)(-19)$[c]		

Compositions by mole fraction:
[a]9.11×10^{-3} $^{14}N_2$, 3.64×10^{-5} CO, balance ^{4}He. Pressure 18.3–21.5 bar.
[b]2.54×10^{-2} $^{14}N_2$, 8.55×10^{-5} CO, balance ^{4}He. Pressure 15.8–23.5 bar.
[c]2.56×10^{-2} $^{14}N_2$, 1.72×10^{-4} CO, balance ^{4}He. Pressure 14.5–17.0 bar.
[d]9.61×10^{-3} $^{15}N_2$, 7.54×10^{-5} CO, balance ^{3}He. Pressure 1.2 bar.

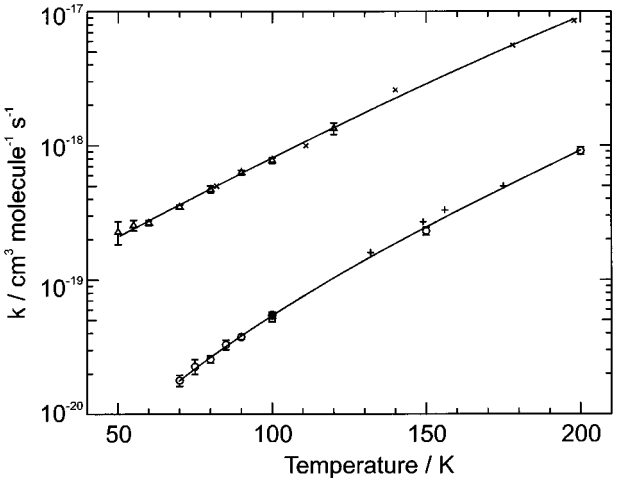

FIG. 1. Experimental rate constants for the vibrational deactivation of $^{14}N_2$ ($v=1$) by ^{4}He and $^{15}N_2$ ($v=1$) by ^{3}He. $^{14}N_2$ ($v=1$)-^{4}He. The present study: (—), (○); [Ref. 16: (+)]. $^{15}N_2$ ($v=1$)-^{3}He. The present study: (—), (△); [Ref. 16 (×)].

The fraction of energy remaining in CO once the coupled pair is formed is given by f_{CO} and the fraction of energy in N_2 is given by f_{N_2}. The rate constants for the deactivation of CO and N_2 by He are denoted by k_{CO-He} and k_{N_2-He}, respectively, χ_{He} denotes the mole fraction of helium in the mixture, k_{rad} is the radiative rate and ρ_{imp} is the rate of deactivation of the coupled pair by impurities present in the gas mixture. The values for k_{rad} and ρ_{imp} are known to within $\pm10\%$. Although the experimental analysis considers the complete set of coupled equations and makes no such approximations, the treatment outlined above is used when designing mixture compositions. By selecting the conditions correctly, it can be ensured that the minimum contribution is achieved to the overall rate from the deactivation of CO($v=1$) by He, by the radiative rate of CO($v=1$) and by impurities deactivating the excited species. It is, however, important to recognize that the fraction of energy remaining in CO must be sufficient to give a good signal-to-noise ratio and that the partial pressure of N_2 should be much less than its vapor pressure at the temperatures at which the experiments are performed. The relaxation rate of N_2 by helium is, at worst, a factor of two faster than that for the deactivation of CO($v=1$) by helium. Rate constants for the latter process are taken from Refs. 1 and 17.

The rate of the *VT* deactivation process is faster than the rate of the radiative processes by, at worst, a factor of 4 with the experiments performed at pressures as high as 22 bar for the $^{14}N_2$–^{4}He system and 2 bar for the $^{15}N_2$–^{3}He system.

Results for the deactivation of $^{14}N_2$ by ^{4}He are presented in Table II and Fig. 1, and for the deactivation of $^{15}N_2$ by ^{3}He. Older results from Ref. 17 are also shown in Fig. 1 for ease of comparison.

III. POTENTIAL ENERGY SURFACE

The interaction PES was calculated *ab initio* by the supermolecule method in the same manner as in our earlier work.[10] In particular, we performed the fourth-order Møller–Plesset perturbation theory (MP4) calculations with full counterpoise corrections. The one-particle basis set was set six from Ref. 10; it consists of $[5s4p3d, 4s3p2d]$ atom-centered contracted Gaussians plus $3s3p2d1f$ bond-centered primitive Gaussians.

We chose a mesh of 14 intermolecular distances R and five angles θ for each of three N_2 bond lengths r. The latter were chosen to be the equilibrium value $r=2.0743a_0$ and the turning points of the classical motion in the $v=1$, $J=0$ vibrotational state of N_2, $r=2.0a_0$, and $2.2a_0$. The mesh in R was denser around the van der Waals minimum than in our earlier work.[10] This mesh results in a total of 210 *ab initio* points on the three-dimensional PES. Of these, 53 points at the equilibrium N_2 bond length were taken from Ref. 10 and 157 points were calculated in this work. The full *ab initio* MP4 potential energy surface is reported in Table III.

It is absolutely crucial to obtain a good analytic representation of the MP4 PES. We made some efforts to find a true three-dimensional representation but were not satisfied with the quality of the fits. We think that *ab initio* calculations at a significantly wider range of r are needed for a true three-dimensional fit. Hence, we fit the points for each fixed N_2 bond length to the functional form of Ref. 10. This is given by

$$V(R,\theta)=V_{SS}(R,\theta)+V_r-V_a(R,\theta), \tag{9}$$

in which V_r and $-V_a$, respectively, are repulsive and attractive terms and V_{SS} is an additional site-site term that is designed to model the small R anisotropy. The site-site term is given by

$$V_{SS}(R,\theta)=\sqrt{R_a}\,\exp(Z-\zeta R_a)+\sqrt{R_b}\,\exp(Z-\zeta R_b) \tag{10}$$

in which Z and ζ are parameters, and R_a and R_b, respectively, are distances from the He nucleus to the two different N nuclei:

TABLE III. MP4 interaction energies for He–N_2 in microhartrees.

	θ				
R/a_0	0.0	22.5	45.0	67.5	90.0
			$r=2.0a_0$		
4.00	67243.98	51098.89	26065.92	12817.48	9445.27
5.00	8525.16	6489.55	3128.21	1290.67	833.22
5.50	2737.18	2040.32	888.33	270.54	123.01
5.75	1478.37	1077.29	418.17	72.62	−6.69
6.00	755.22	527.94	158.70	−27.84	−67.84
6.25	348.85	222.78	21.91	−73.40	−91.36
6.50	127.30	59.53	−44.97	−89.13	−95.14
6.75	11.92	−22.74	−73.12	−89.49	−89.36
7.00	−43.64	−59.87	−80.65	−82.62	−79.63
7.25	−66.40	−72.64	−77.87	−72.95	−68.87
7.50	−71.84	−72.94	−70.50	−62.79	−58.54
8.00	−61.97	−59.60	−52.75	−44.77	−41.26
9.00	−32.92	−30.97	−26.39	−22.02	−20.28
10.00	−16.52	−15.59	−13.38	−11.30	−10.47
			$r=2.0743a_0$		
4.00	71483.88	53803.13	26940.76	13058.91	9583.21
5.00	9105.26	6881.82	3267.29	1338.33	867.84
5.50	2935.41	2174.55	935.48	287.30	136.16
5.75	1590.81	1152.90	443.88	81.62	0.67
6.00	817.13	568.91	171.65	−23.62	−64.19
6.25	381.44	243.66	27.49	−72.02	−89.95
6.50	143.19	69.04	−43.48	−89.33	−95.05
6.75	18.55	−19.46	−73.78	−90.51	−89.98
7.00	−41.98	−59.85	−82.33	−83.99	−80.58
7.25	−67.24	−74.21	−79.92	−74.42	−69.94
7.50	−73.82	−75.15	−72.6	−64.21	−59.61
8.00	−64.35	−61.84	−54.52	−45.92	−42.16
9.00	−34.38	−32.29	−27.35	−22.65	−20.80
10.00	−17.29	−16.27	−13.86	−11.63	−10.74
			$r=2.2a_0$		
4.00	79120.03	58591.07	28435.69	13414.45	9745.31
5.00	10171.99	7594.65	3511.00	1413.96	918.67
5.50	3303.12	2421.02	1019.32	314.75	156.50
5.75	1800.30	1292.49	490.01	96.59	12.37
6.00	932.98	645.01	195.16	−16.45	−58.16
6.25	442.72	282.72	37.81	−69.55	−87.51
6.50	173.28	87.00	−40.57	−89.56	−94.74
6.75	31.23	−13.15	−74.80	−92.15	−90.88
7.00	−38.67	−59.67	−85.24	−86.27	−82.06
7.25	−68.68	−77.02	−83.58	−76.89	−71.65
7.50	−77.45	−79.20	−76.37	−66.63	−61.34
8.00	−68.82	−66.04	−57.73	−47.93	−43.65
9.00	−37.18	−34.78	−29.13	−23.78	−21.66
10.00	−18.74	−17.55	−14.80	−12.24	−11.22

$$R_a^2 = R^2 + \frac{r^2}{4} - rR\cos\theta,$$
$$R_b^2 = R^2 + \frac{r^2}{4} + rR\cos\theta, \tag{11}$$

where r is the fixed bond length of the N_2 molecule. The repulsive term is given by

$$V_r(R,\theta) = \exp[A(\theta) - b(\theta)R + \gamma(\theta)\ln R], \tag{12}$$

where the angle dependence of the parameters A, b, and γ is given by

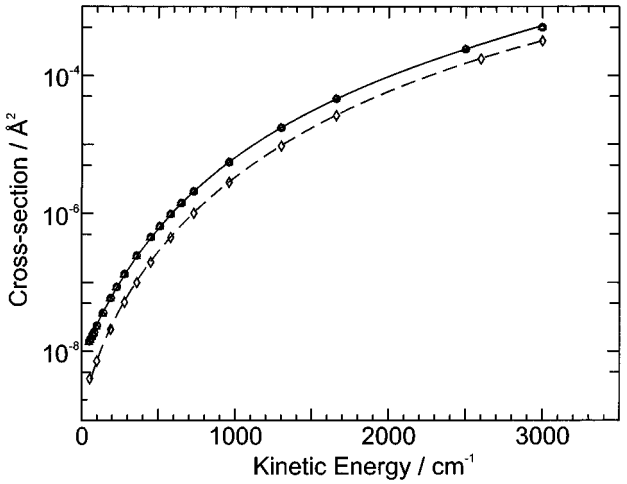

FIG. 2. Cross sections for the vibrational deactivation of $^{14}N_2$ ($v=1, J$) by ^{3}He summed over all final rotational states of N_2. Initial $^{14}N_2$ ($v=1, J=0$): (○); Initial $^{14}N_2$ ($v=1, J=1$): (△); Calculation of Ref. 9 from initial $^{14}N_2$ ($v=1, J=0$): (◇).

$$A(\theta) = A_0 + A_2P_2(\cos\theta) + A_4P_4(\cos\theta)$$
$$b(\theta) = b_0 + b_2P_2(\cos\theta) + b_4P_4(\cos\theta) \tag{13}$$
$$\gamma(\theta) = \gamma_0 + \gamma_2P_2(\cos\theta) + \gamma_4P_4(\cos\theta)$$

in which P_2 and P_4 are Legendre polynomials. The attractive term is given by a truncated, damped, multipole expansion:

TABLE IV. Parameters (in atomic units) for the MP4F fit to the *ab initio* PES for He–N_2 at different N_2 bond lengths (r).

Fit parameters	r/a_0		
	2.0	2.0743	2.2
A_0	2.90038	2.92808	2.95358
A_2	7.16514E−01	7.51863E−01	9.11216E−01
A_4	1.12334	1.09543	1.07881
b_0	2.37623	2.37630	2.38034
b_2	2.11264E−01	2.18521E−01	2.20705E−01
b_4	2.74155E−01	−2.78975E−01	−2.79747E−01
G_0	1.98597	1.99498	1.99858
G_2	1.09078	1.10519	1.05817
G_4	−1.60141	−1.60122	−1.59990
ρ_0	1.27265	1.27435	1.26607
ρ_2	3.54205E−01	3.86039E−01	4.07788E−01
Z	1.80300E−01	1.83154E−01	1.76151E−01
ζ	2.02043	2.02705	1.93547
C_6^0	9.41032	9.74931	1.02218E+01
C_6^2	1.23081	1.44401	1.65207
C_8^0	1.92408E+02	2.01405E+02	2.32280E+02
C_8^2	1.61471E+02	1.74587E+02	1.95267E+02
C_8^4	−6.16708	−1.72637E+01	1.53978E+01
C_{10}^0	1.15605E+04	1.16056E+04	1.18847E+04
C_{10}^2	1.16074E+04	1.17802E+04	1.32383E+04
C_{10}^4	4.43302E+03	5.41505E+03	4.08916E+03
C_{10}^6	0.0	0.0	0.0

$$V_a(R,\theta)=g_6(\rho R)\,\frac{C_6(\theta)}{R^6}+g_8(\rho R)\,\frac{C_8(\theta)}{R^8}+g_{10}(\rho R)\,\frac{C_{10}(\theta)}{R^{10}} \tag{14}$$

where the angle dependence of the long-range (dispersion+induction) coefficients is given by

$$\begin{aligned}C_6(\theta)&=C_6^0+C_6^2P_2(\cos\theta)\\ C_8(\theta)&=C_8^0+C_8^2P_2(\cos\theta)+C_8^4P_4(\cos\theta)\\ C_6(\theta)&=C_{10}^0+C_{10}^2P_2(\cos\theta)+C_{10}^4P_4(\cos\theta)\\ &\quad+C_{10}^6P_6(\cos\theta)\end{aligned} \tag{15}$$

and the damping functions are those introduced by Douketis *et al.*[18]

$$g_n(\rho R)=[1-\exp(-2.1\rho R/n-0.109p^2R^2/\sqrt{n})]^n \tag{16}$$

with an angle dependent damping parameter

$$\rho=\rho_0+\rho_2P_2(\cos\theta). \tag{17}$$

C_{10}^6 was set to zero because its inclusion does not have a significant impact on the fit. Thus, at each r, we fit 70 points using 21 parameters. This relatively high ratio of 3.33 points per parameter helps to ensure that the fit does not introduce unphysical kinks or oscillations between the *ab initio* points. The fitting procedure was the same as the one we used previously. The three fits together have an absolute error that averages 0.53%. The largest fitting errors occur at intermolecular distances R shorter than $5a_0$; fortunately, this short-range region of the PES is not very important for most of the physical properties normally computed from a van der Waals PES. The parameters of the best fit are listed in Table IV. Note that the parameters for $r=2.0743a_0$ are slightly different from those of Hu and Thakkar because they fitted fewer *ab initio* points than we did.

Given the three rigid-rotor fits, specification of an interpolation method for other rotor lengths is required to define a three-dimensional PES. The range of r is so small that quadratic interpolation is sufficiently accurate. We found that calculation of the interaction energy from the three rigid-rotor fits followed by quadratic Lagrangian interpolation to the desired rotor length was significantly more well-conditioned than calculation of the interaction energy using our analytic form with parameters interpolated to the desired rotor length. The three-dimensional PES obtained by the preferred interpolation procedure is referred to as the MP4F3D surface to emphasize the subtle but important distinction between our *ab initio* points and the fit. A FORTRAN subroutine that calculates the MP4F3D PES is freely available by anonymous ftp from `ftp://okapi.chem.unb.ca/pub/imf/n2he/mp4f3d.for`.

IV. SCATTERING CALCULATIONS

The methods adopted for these atom-diatom scattering calculations have been discussed in previous publications.[4,9,19] The collision pair was treated within the coupled-states (CS) approximation[20] using the molecular scattering program MOLSCAT.[21] The hybrid log-derivative/Airy propagator[22] was used for the propagation of the wave functions. Stringent convergence testing was performed in order to ensure that the calculated cross sections were converged to well within a 1% tolerance. The $o\mathrm{N_2}$ and $p\mathrm{N_2}$ nuclear spin isomers were treated independently with 16 rotational states included in the basis set above both the $v=0$ and $v=1$ thresholds and 11 rotational states in the vibrationally closed channel, $v=2$. This basis set corresponds to a maximum of $J=30$ in $v=0$ and 1 for $p\mathrm{N_2}$ and $J=31$ in $v=0$ and 1 for $o\mathrm{N_2}$. The basis set energies were calculated using $\omega_e=2358.57\ \mathrm{cm^{-1}}$, $\omega_e x_e=14.30\ \mathrm{cm^{-1}}$, $B_e=1.99824\ \mathrm{cm^{-1}}$ and $\alpha_e=0.0173\ \mathrm{cm^{-1}}$ for $^{14}\mathrm{N_2}$ and $\omega_e=2279.77\ \mathrm{cm^{-1}}$, $\omega_e x_e=13.82\ \mathrm{cm^{-1}}$, $B_e=1.86542\ \mathrm{cm^{-1}}$ and $\alpha_e=0.01557\ \mathrm{cm^{-1}}$ for $^{15}\mathrm{N_2}$.[23] The maximum propagation distance was 20 Å and convergence was ensured with respect to the propagator step size. A maximum partial wave of $L=10$ was found necessary for the resonance searching at low impact energies and the scattering calculation was performed for all partial waves up to this angular momentum state. For impact energies in the range $20-100\ \mathrm{cm^{-1}}$, contributions from partial waves up to $L=21$ were considered with the calculation performed for partial waves from 1 to 21 in steps of 2. The final scattering cross section was multiplied by a factor of two to account for the step size. Contributions from partial waves up to $L=38$, in steps of 4, were required for convergence of the cross sections in the impact energy range $100-1500\ \mathrm{cm^{-1}}$ while contributions up to $L=58$ were included for energies above this range.

In order to achieve convergence of the thermally averaged rate constants at low temperatures, it was found necessary to calculate the scattering cross sections at a large number of impact energies in the range $20-100\ \mathrm{cm^{-1}}$. This gives accurate thermal averaging down to 30 K. Below this temperature, the resonance structure contributes significantly to the thermally averaged rate constants and the cross sections were calculated over a fine grid of collision energies in order to enable the accurate calculation of the relaxation rate constants. Rate constants were calculated for the relaxation of each initial rotational state of $\mathrm{N_2}$ by performing the thermal average over the kinetic energy distribution at a temperature T

$$\begin{aligned}&k_{\mathrm{CS}}(v=1,J\rightarrow v=0;T)\\ &=\left(\frac{8}{\pi\mu(k_BT)^3}\right)^{1/2}\int_0^\infty\sigma_{\mathrm{CS}}(v=1,J\rightarrow v=0;E_{\mathrm{Kin}})\\ &\quad\times\exp(-E_{\mathrm{Kin}}/k_BT)E_{\mathrm{Kin}}dE_{\mathrm{Kin}}.\end{aligned} \tag{18}$$

The scattering cross section summed over all final rotational states is denoted by $\sigma_{\mathrm{CS}}(v=1,J\rightarrow v=0)$, with the scattering calculations performed at impact energies E_{Kin}. The reduced mass of the collision pair is denoted by μ. Rate constants for the relaxation of $n\mathrm{N_2}(v=1)$ were calculated by weighting the rate constants for relaxation from initial rotational states assuming a Boltzmann rotational distribution,

TABLE V. The ^{3}He and ^{4}He–$^{14}N_2$ systems: Relaxation cross sections from $J=0$ (in Å^2).

Kinetic energy (cm^{-1})	$\sigma_{^3He-^{14}N_2}$ This calculation	$\sigma_{^3He-^{14}N_2}$ Reference 9	$\sigma_{^4He-^{14}N_2}$ This calculation	$\sigma_{^4He-^{14}N_2}$ Reference 9
5.0	0.290(−7)	0.497(−8)	0.128(−8)	0.278(−9)
10.0	0.217(−7)	⋯	0.152(−8)	⋯
15.0	0.144(−7)	0.297(−8)	0.936(−9)	0.171(−9)
20.0	0.132(−7)	⋯	0.890(−9)	⋯
30.0	0.127(−7)	⋯	0.840(−9)	⋯
40.0	0.129(−7)	⋯	0.919(−9)	⋯
50.0	0.141(−7)	0.400(−8)	0.100(−8)	⋯
60.0	0.154(−7)	⋯	0.112(−8)	⋯
70.0	0.171(−7)	⋯	0.127(−8)	⋯
80.0	0.190(−7)	⋯	0.144(−8)	⋯
100.0	0.238(−7)	0.730(−8)	0.188(−8)	0.529(−9)
140.0	0.364(−7)	⋯	0.308(−8)	0.964(−9)
190.0	0.599(−7)	0.209(−7)	0.547(−8)	0.183(−8)
230.0	0.866(−7)	⋯	0.834(−8)	0.293(−8)
280.0	0.133(−6)	0.518(−7)	0.136(−7)	0.499(−8)
360.0	0.246(−6)	0.100(−6)	0.274(−7)	0.107(−7)
450.0	0.455(−6)	0.197(−6)	0.550(−7)	0.228(−7)
510.0	0.659(−6)	⋯	0.838(−7)	0.359(−7)
580.0	0.982(−6)	0.450(−6)	0.132(−6)	0.583(−7)
650.0	0.142(−5)	⋯	0.200(−6)	0.913(−7)
730.0	0.210(−5)	0.101(−5)	0.312(−6)	0.146(−6)
960.0	0.556(−5)	0.284(−5)	0.937(−6)	0.472(−6)
1300.0	0.175(−4)	0.953(−5)	0.343(−5)	0.187(−5)
1660.0	0.460(−4)	0.262(−4)	0.102(−4)	0.591(−5)
2500.0	0.241(−3)	0.174(−3)	0.663(−4)	0.423(−4)
3000.0	0.502(−3)	0.318(−3)	0.152(−3)	0.102(−3)

TABLE VII. The ^{3}He and ^{4}He–$^{15}N_2$ systems: Relaxation cross sections from $J=0$ (in Å^2).

Kinetic energy (cm^{-1})	$\sigma_{^3He-^{14}N_2}$ This calculation	$\sigma_{^3He-^{14}N_2}$ Reference 9	$\sigma_{^4He-^{14}N_2}$ This calculation	$\sigma_{^4He-^{14}N_2}$ Reference 9
5.0	0.493(−7)	0.662(−8)	0.264(−8)	0.423(−9)
10.0	0.106(−6)		0.182(−8)	⋯
15.0	0.211(−7)	0.464(−8)	0.125(−8)	0.256(−9)
20.0	0.176(−7)	⋯	0.118(−8)	⋯
30.0	0.172(−7)	⋯	0.118(−8)	⋯
40.0	0.179(−7)	⋯	0.123(−8)	⋯
50.0	0.191(−7)	0.537(−8)	0.137(−8)	0.355(−9)
60.0	0.208(−7)	⋯	0.154(−8)	⋯
70.0	0.230(−7)	⋯	0.175(−8)	⋯
80.0	0.256(−7)	⋯	0.198(−8)	⋯
100.0	0.322(−7)	0.985(−8)	0.259(−8)	0.731(−9)
140.0	0.492(−7)	⋯	0.426(−8)	⋯
190.0	0.812(−7)	0.292(−7)	0.758(−8)	0.254(−8)
230.0	0.118(−6)	⋯	0.116(−7)	⋯
280.0	0.180(−6)	0.707(−7)	0.189(−7)	0.695(−8)
360.0	0.334(−6)	0.139(−6)	0.382(−7)	0.150(−7)
450.0	0.617(−6)	0.268(−6)	0.766(−7)	0.318(−7)
510.0	0.893(−6)	⋯	0.117(−6)	⋯
580.0	0.133(−5)	0.612(−6)	0.183(−6)	0.810(−7)
650.0	0.192(−5)	⋯	0.278(−6)	⋯
730.0	0.283(−5)	0.137(−5)	0.432(−6)	0.203(−6)
960.0	0.745(−5)	0.381(−5)	0.129(−5)	0.649(−6)
1300.0	0.233(−4)	0.126(−4)	0.469(−5)	0.254(−5)
1660.0	0.604(−4)	0.344(−4)	0.138(−4)	0.793(−5)
2500.0	0.309(−3)	0.188(−3)	0.875(−4)	0.552(−4)
3000.0	0.638(−3)	0.401(−3)	0.199(−3)	0.131(−3)

and by weighting the odd and even rotational states according to the ratios predicted by nuclear spin statistics.

Relaxation cross sections and rate constants have been calculated for the four isotopic systems: $^{14}N_2$–^{3}He, $^{14}N_2$–^{4}He, $^{15}N_2$–^{3}He, and $^{15}N_2$–^{4}He. The results of these calculations are presented in Tables V–VIII and in Figs. 2–4. The results of the resonance searches for initial rotational states $J=0$ and 1 are presented in Figs. 5 and 6 with their influence on the thermally averaged rate constants shown in Fig. 7.

V. DISCUSSION

Agreement between theory and experiment is excellent for all the systems considered. The theoretical values of the relaxation rate constants show a deviation of less than the error bar on the experimental values at all temperatures for which data are available. Hu and Thakkar suggested that the elastic part of the MP4F potential, calculated at one fixed N_2 bond length and which we have used in the present study, is accurate to within 10% of the true potential energy surface, within the Born–Oppenheimer approximation. On the

TABLE VI. The $^{14}N_2$–^{3}He and $^{14}N_2$–^{4}He systems: Relaxation rate constants (in units of $cm^3\,mol^{-1}\,s^{-1}$).

Temperature (K)	$^{14}N_2$–^{4}He $k_{Exp.}$	$^{14}N_2$–^{4}He k_{CS}	$^{14}N_2$–^{4}He $k_{CS}/k_{Exp.}$	$^{14}N_2$–^{4}He $k_{Ref.\ 9}$	$^{14}N_2$–^{3}He $k_{Exp.}$	$^{14}N_2$–^{3}He k_{CS}	$^{14}N_2$–^{3}He $k_{CS}/k_{Exp.}$	$^{14}N_2$–^{3}He $k_{Ref.\ 9}$
35	⋯	6.01(−21)	⋯	1.47(−21)	⋯	9.13(−20)	⋯	2.30(−20)
40	⋯	7.19(−21)	⋯	1.89(−21)	⋯	1.06(−19)	⋯	2.84(−20)
50	⋯	1.04(−20)	⋯	3.05(−21)	⋯	1.43(−19)	⋯	4.25(−20)
70	1.8(−20)	2.17(−20)	1.1	7.46(−21)	⋯	2.64(−19)	⋯	9.06(−20)
85	3.3(−20)	3.74(−20)	1.1	1.38(−20)	⋯	4.14(−19)	⋯	1.53(−19)
100	5.4(−20)	6.10(−20)	1.1	2.43(−20)	6.2(−19)	6.26(−19)	1.0	2.49(−19)
150	2.8(−19)	2.66(−19)	1.1	1.20(−19)	2.0(−18)	2.19(−18)	1.1	1.00(−18)
200	8.7(−19)	8.83(−19)	1.0	4.57(−19)	6.0(−18)	6.15(−18)	1.0	3.09(−18)
250	2.6(−18)	2.44(−18)	0.94	1.38(−18)	1.5(−17)	1.48(−17)	1.0	7.94(−18)
290	4.9(−18)	4.88(−18)	1.0	3.02(−18)	2.6(−17)	2.73(−17)	1.1	1.58(−17)

TABLE VIII. The $^{15}N_2$–^{3}He and $^{15}N_2$–^{4}He systems: Relaxation rate constants (in units of $cm^3\,mol^{-1}\,s^{-1}$).

Temperature (K)	$^{15}N_2$–^{4}He				$^{15}N_2$–^{3}He			
	$k_{Exp.}$	k_{CS}	$k_{CS}/k_{Exp.}$	$k_{Ref.\ 9}$	$k_{Exp.}$	k_{CS}	$k_{CS}/k_{Exp.}$	$k_{Ref.\ 9}$
35	⋯	8.20(−21)	⋯	1.89(−21)	⋯	1.28(−19)	⋯	2.76(−20)
40	⋯	9.83(−21)	⋯	2.49(−21)	⋯	1.48(−19)	⋯	3.46(−20)
50	⋯	1.42(−20)	⋯	3.95(−21)	2.1(−19)	1.99(−19)	0.95	5.33(−20)
70	⋯	2.97(−20)	⋯	9.90(−21)	3.5(−19)	3.59(−19)	1.0	1.18(−19)
85	⋯	5.10(−20)	⋯	1.85(−20)	5.4(−19)	5.59(−19)	1.0	2.01(−19)
100	⋯	8.32(−20)	⋯	3.28(−20)	8.3(−19)	8.41(−19)	1.0	3.29(−19)
150	3.8(−19)	3.61(−19)	0.95	1.70(−19)	3.0(−18)	2.91(−18)	0.97	1.35(−18)
200	1.3(−18)	1.19(−18)	0.92	6.46(−19)	8.7(−18)	8.13(−18)	0.93	3.89(−18)
250	3.2(−18)	3.27(−18)	1.1	1.86(−18)	2.0(−17)	1.95(−17)	0.98	9.55(−18)
290	6.3(−18)	6.51(−18)	1.0	4.17(−18)	3.6(−17)	3.57(−17)	1.0	1.82(−17)

basis of the quantitative agreement between the theory and experiment observed in the present study, this estimate appears to be vindicated. The calculation of vibrationally inelastic relaxation rate constants is a severe test of the accuracy of the *ab initio* methods which are used to generate the potential. This is because the entire reaction surface is sampled, and there is an additional internal degree of freedom introduced by the inelastic scattering calculations.

Experimental values of the vibrationally inelastic rate constants have been measured down to a temperature of 50 K for the $^{15}N_2$–^{3}He system and cannot readily be extended below this temperature. The rate constants for the endothermic transfer of the vibrational quantum from CO to $^{15}N_2$ decrease rapidly below 80 K. The vapor pressure of N_2 also decreases rapidly[24] and this limits the partial pressure of N_2 which can be used. In consequence, the rate of formation of the CO/N_2 coupled pair becomes prohibitively small for an accurate determination of the N_2–He rate constants below 50 K. In addition, the requirement that the deactivation rate for the process being studied be substantially faster than the other competing processes demands that helium-3 pressures in excess of 2 bar be used. These two problems are considerably more limiting for the deactivation of $^{14}N_2(v=1)$ by ^{4}He: the experimental data for this system are extended down to a temperature of 70 K. However, a comparison of the experimental results and the calculated rate constants for the $^{15}N_2$–^{3}He system at 50 K does enable firm conclusions to be drawn about the accuracy of the low repulsive wall of the MP4F3D surface at interaction energies as low as 35 cm^{-1}. Such a comparison shows that the good agreement between the theoretically calculated rate constants and the experimentally measured values persists down to 50 K. At the lowest temperatures of the experimental measurements, the rate constants for the deactivation of $^{14}N_2(v=1)$ by ^{4}He are smaller than the theoretical values while for the deactivation of $^{15}N_2(v=1)$ by ^{3}He, the measured values are larger than those calculated theoretically. In both cases, the theoretical values remain within the experimental error and the discrepancy is not significant.

In order to reproduce the results of beam scattering, transport phenomena, and relaxation phenomena, Beneventi *et al.*[11] concluded that the anisotropy of any accurate inter-

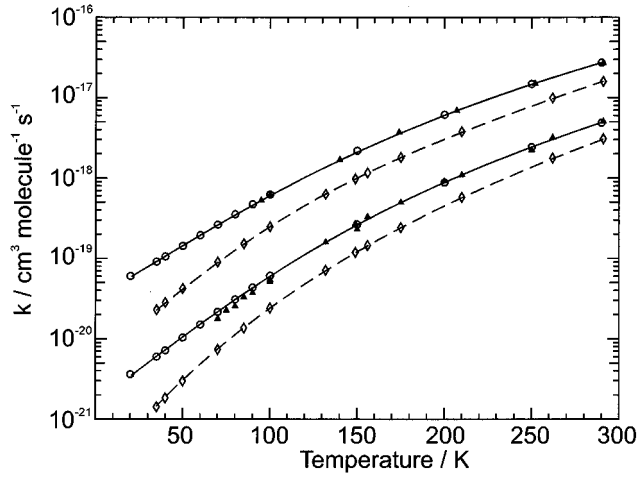

FIG. 3. Rate constants for the vibrational deactivation of $^{14}N_2$ ($v=1, J$) by ^{3}He and ^{4}He (the lighter mass system having the larger rate constant). Open symbols, the present calculation: (—), (○); calculation of Ref. 9 : (– –), (◇). Filled symbols, experiment of Ref. 16 and this study: (△).

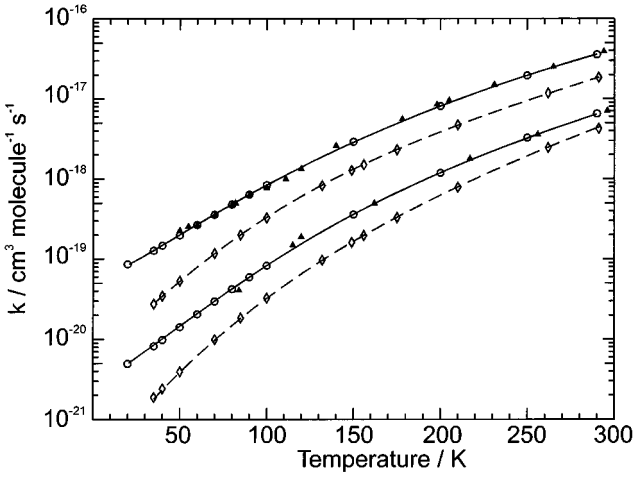

FIG. 4. Rate constants for the vibrational deactivation of $^{15}N_2$ ($v=1, J$) by ^{3}He and ^{4}He (the lighter mass system having the larger rate constant). Open symbols, the present calculation: (—), (○); calculation of Ref. 9 : (– –), (◇). Filled symbols, experiment of Ref. 6 and this study : (△).

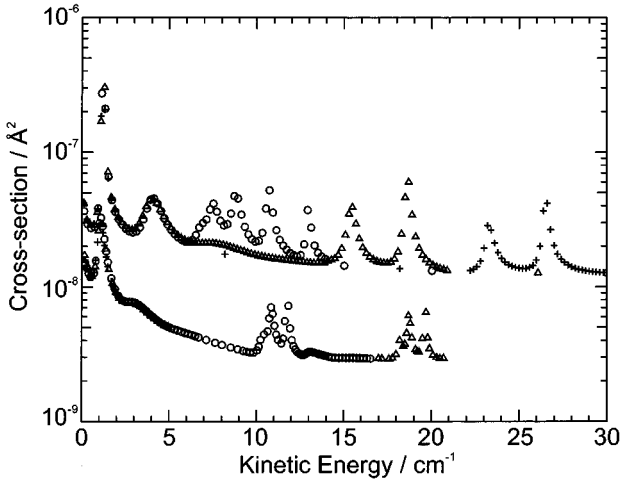

FIG. 5. Low impact energy cross sections for the vibrational deactivation of $^{14}N_2$ ($v = 1, J$) by ^{3}He summed over all final rotational states of N_2 (upper curves): initial $^{14}N_2$ ($v = 1, J = 0$): (○); initial $^{14}N_2$ ($v = 1, J = 1$): (△); initial $^{14}N_2$ ($v = 1, J = 2$):(+). Calculation of Ref. 9 (lower curves): initial $^{14}N_2$ ($v = 1, J = 0$): (○); initial $^{14}N_2$ ($v = 1, J = 1$): (△).

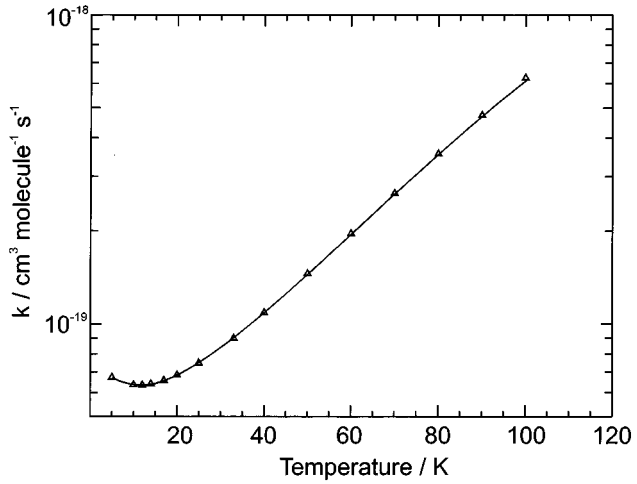

FIG. 7. Rate constants for the vibrational deactivation of $^{14}N_2$ ($v = 1, J$) by ^{3}He at low temperatures. The present calculation: (—), (△).

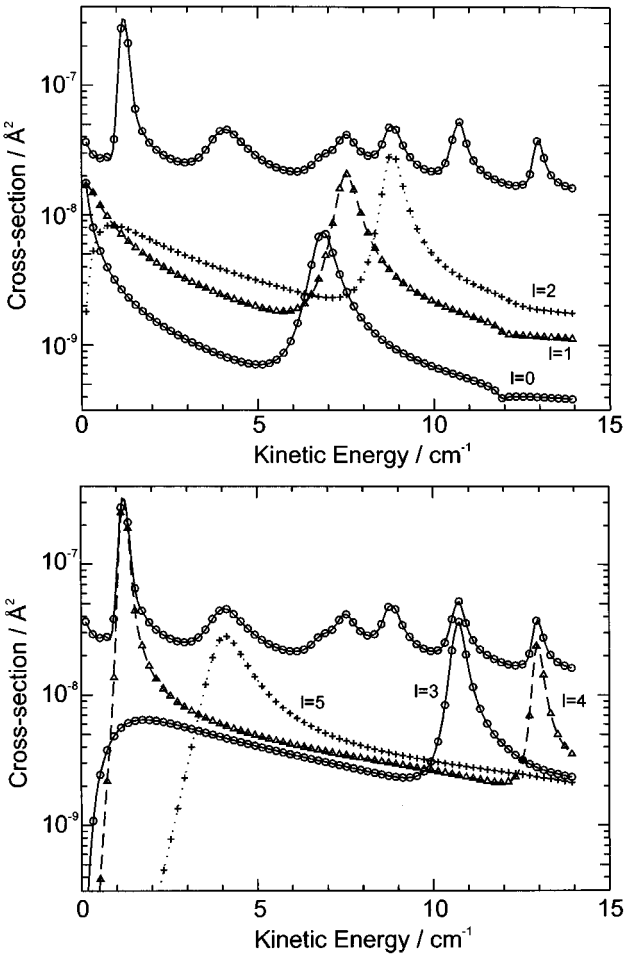

FIG. 6. Low impact energy cross sections for the vibrational deactivation of $^{14}N_2$ ($v = 1, J = 0$) by ^{3}He summed over all final rotational states of N_2: partial wave contributions.

action potential should closely resemble that of Bowers *et al.*[25] in the region of the low repulsive wall, a condition which is fulfilled by the MP4F3D potential.[10] That the relaxation rate constants in the temperature range $50\,\mathrm{K} < T < 100\,\mathrm{K}$ are well reproduced by the MP4F3D potential, indicates that it possesses the correct well depth, potential gradient, and anisotropy at small interaction energies.

Given the good agreement between theoretical and experimental values of second virial coefficients for this system, and the agreement found in the present work, it seems safe to assume that the interaction potential is sufficiently accurate to make quantitative predictions of the behavior of the N_2–He systems. Below 20 K, the theoretical values of the rate constants show a small, but readily identifiable upturn which becomes pronounced below 15 K. Since we regard this interaction surface as reliable, and the CS treatment includes all angular momentum contributions which are likely to be significant for this system, it is likely that this predicted upturn in rate constants would be seen if this temperature range was accessible to our experimental method.

Our previous calculations of the relaxation rate constants for the N_2–He systems[9] showed a systematic discrepancy between theory and experiment, which we attributed to deficiencies in the CEPA interaction potential surface which was used. It is therefore instructive to examine the features of the CEPA potential and the MP4F3D potential which are likely to be the causes of these discrepancies. A comparison of the attractive well region and the low impact energy repulsive wall is shown in Fig. 8. Hu and Thakkar present an extensive comparison of N_2–He interaction potentials in terms of the differences in well depths and radial positions of the point at which the interaction potential attains a zero value at the T-shaped and linear configurations. The difference between the zero-value point of the surfaces at the T shape and linear configurations is a rough guide to the degree of anisotropy of the surface, which plays a crucial role in determining the details of angular momentum coupling. The repulsive walls of the two potential energy surfaces are very similar in shape

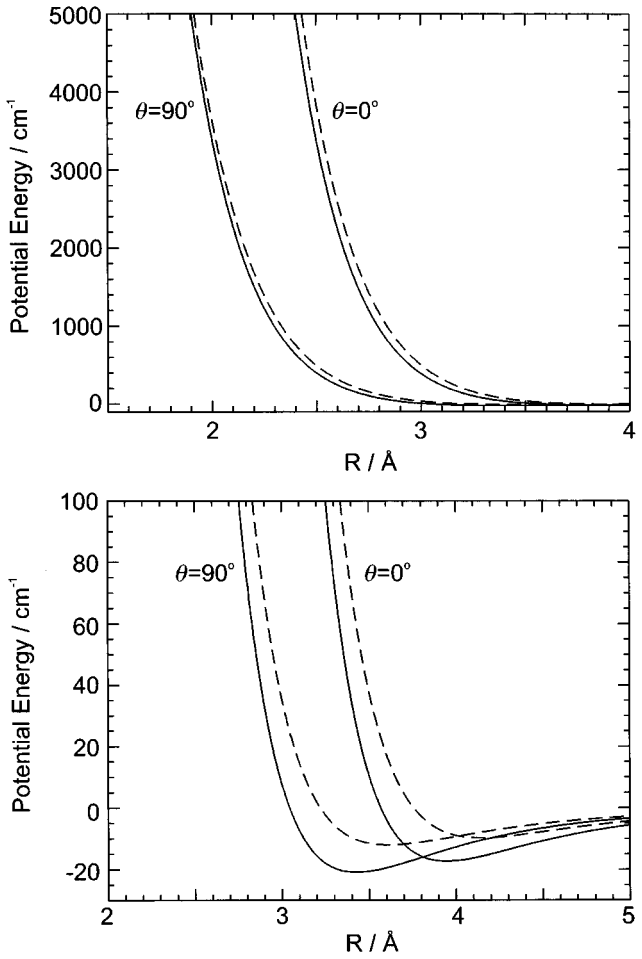

FIG. 8. Comparison of the MP4F and CEFA potential energy surfaces in the attractive well region and on the low repulsive wall for the linear and (T-shaped geometries: MP4F surface: (—). CEPA: (– –).

and a small translation of the CEPA surface to shorter intermolecular separation by as little as 0.02 Å would be sufficient to very nearly overlay the two potential energy surfaces in the repulsive region. However, this is not able to explain the quantitative difference of the rate constants calculated from the two surfaces. The scattering cross sections are stable to within 2% with respect to an artificial translation of the potential energy surface of up to 0.5 Å. The convergence of the two calculations in the higher temperature limit suggests that the discrepancy results from the influence of the attractive well on the phase shift between initial and final states.

In Table IX, we examine the sensitivity of the scattering cross sections to small changes in the potential energy surface. Parametric changes in the damping function [Eq. (16)], were made by weighting the constant ρ^2, which had the effect of modifying the anisotropy of the PES. Comparing the linear and T-shaped collisional configurations, the modification results in a difference in the position at which the PES changes sign of ΔR_0 Å, a difference in the position of the minimum value of the potential of ΔR_m, and a change in difference in the minimum of energy in the two configurations of ΔE cm^{-1}. Such a simple choice for the anisotropy

TABLE IX. The dependence of the scattering cross sections (in Å^2) on the anisotropy of the potential energy surface.

		Surface parameters		
Kinetic energy (cm^{-1})	Initial (J)	$\Delta R_0=0.56$ Å $\Delta R_m=0.55$ Å $\Delta E=4.8$ cm^{-1} ρ^{2a}	$\Delta R_0=0.47$ Å $\Delta R_m=0.44$ Å $\Delta E=1.8$ cm^{-1} $(2\rho^2)/3$	$\Delta R_0=0.43$ Å $\Delta R_m=0.39$ Å $\Delta E=5.0$ cm^{-1} $(\rho^2)/2$
50 ($l=2$)	0	10.48	9.14[b]	7.85[b]
			0.90	0.75
50 ($l=3$)	0	13.50	11.80	10.13
			0.87	0.75
250 ($l=2$)	0	5.56	5.13	4.65
			0.92	0.84
40 ($l=2$)	2	10.19	8.74	7.43
			0.86	0.73
40 ($l=3$)	2	13.07	11.21	9.52
			0.86	0.73
240 ($l=2$)	2	5.30	4.86	4.39
			0.92	0.83
15 ($l=2$)	4	18.86	14.45	11.52
			0.77	0.61
15 ($l=3$)	4	22.48	17.87	14.21
			0.80	0.61
215 ($l=2$)	4	5.41	4.26	3.82
			0.79	0.71

[a]Damping parameter for R^2 term in damping function.
[b]The second number of each pair is the cross section expressed as a fraction of the cross section calculated on the MP4F3D surface.

parameters is possible only because of the high symmetry of the N_2 molecule, for which the linear and T-shaped configurations represent well-defined limiting cases of the potential energy surface, in which the angular gradients of the surface must vanish.

The impact energies were chosen to represent dominant contributions to the relaxation rate constants in the high and low temperature limits. For all energies considered, the fractional change in the cross sections is not strongly dependent on the initial state angular momentum. There is a uniform decrease in the cross sections as the value of the damping parameter is decreased, reflecting the gradual removal of the anisotropy of the attractive part of the interaction surface. The greatest relative change in the cross sections is found when the damping parameter is chosen to be $\rho^2/2$, for which the nominal anisotropy of the surface is smallest. Moreover, this change in the cross sections is remarkably uniform for all values of the kinetic energy and for all initial state angular momenta, indicating that a change in the anisotropy will have the effect of causing a uniform change in the relaxation rate constants. It appears likely that the apparently constant ratio between the present results and those calculated using the CEPA interaction surface[9] may be attributed mainly to a difference in the anisotropy of the attractive well of the two surfaces.

The divergence of the calculated rate constants obtained from the two potential energy surfaces at low temperatures can be attributed to the vastly different behavior of the cross sections at low impact energies. The Feshbach resonances

found in the scattering cross sections at collision energies up to 40 cm^{-1} from the CEPA surface[9] are also found to occur in the relaxation cross sections calculated from the MP4F3D surface at similar impact energies. The reason for this is that the threshold energies are the same in the two scattering calculations and the short range anisotropic part of the interaction potential is similar for the two surfaces.[26] Thus vibrationally inelastic processes, such as those given below and as suggested by Toennies and co-workers[27,28] for purely rotationally inelastic scattering, will be equally likely on the two surfaces

$$[N_2(v=1,j=0)+He]_{l=J}\begin{cases}\rightarrow[N_2(v=1,j=2)He]_{l_c=J+2} & \rightarrow \\ \rightarrow[N_2(v=1,j=2)He]_{l_c=J} & \rightarrow \\ \rightarrow[N_2(v=1,j=2)He]_{l_c=J-2} & \rightarrow \\ \rightarrow \text{direct} & \rightarrow\end{cases} [N_2(v=0,j=0)+He]_{l=J}. \tag{19}$$

However, the resonances are much broader and stronger in amplitude on the MP4F3D surface than on the CEPA surface. At least in part, the larger amplitude and broader width of these resonances must result from the deeper attractive well of the MP4F3D surface. That the larger well depth is responsible for the larger amplitude and width of the scattering resonances has been considered in previous publications.[6,7] More bound states and quasibound states may be accommodated and more impact energies and incoming orbital angular momenta may result in resonances.

The anisotropy of the interaction surface also has an influence on the magnitude of the scattering resonances. In this respect a comparison with the CO($v=1$)-He system is instructive. The CO–He well depth of 23.7 cm^{-1} (Ref. 33) is not much greater than that of 21.4 cm^{-1} for N_2–He from the MP4F3D surface. However, the upturn in the relaxation rate constants for the CO–He system is calculated to occur below 25 K (Ref. 34) and as shown in Fig. 7, that for N_2–He is calculated to occur at 14 K. This points to the importance of the anisotropy in the potential in enabling resonances in the cross sections and the consequent upturns in the deactivation rate constants. Based on this argument it is likely that the upturn in the rate constants for the N_2–H_2 systems will occur at a temperature appreciably below that of 60 K at which upturns have been observed for CO–H_2. This makes it unlikely that we shall be able to observe experimentally the upturns in rate constants for the N_2–H_2 systems. Further theoretical and experimental studies will be made for these collision partners.

The importance of low impact energy resonances and their contribution to low temperature rate constants has been the subject of much debate. Experimental studies suggest that the low impact energy regime fosters the formation of metastable or van der Waals complexes.[29–32] These long-lived complexes allow multiple collisions to occur and may strongly enhance the vibrational relaxation process. Theoretical studies[26–28,35–37] have considered both types of complex formation for vibrational enhancement and their influence on open-channel (shape)[38] and closed-channel (Feshbach) resonances.[26] We have recently published a study of near-resonant vibration-to-vibration energy transfer at low temperatures where the formation of van der Waals complexes and trapping of the collision pair by collision with a third body is thought to occur.[39] We conclude that for these VT transfers, the collision complex may be the formation of a metastable state which exists long enough to enhance the probability of vibrational energy transfer. The resonances result from Feshbach closed-channel couplings and from open channel or orbiting shape resonances which arise from the penetration of the effective potential energy barrier.

ACKNOWLEDGMENTS

We wish to thank the HPCI Grand Challenge Consortium, G1ep (Chemical Reactions and Energy Exchange Processes), EPSRC Grant 41656, for enabling these calculations to be performed on the Edinburgh Cray T3D. H.M.Q. wishes to acknowledge the support of an EPSRC Advanced Fellowship and we wish to thank EPSRC for providing a research grant for the experimental work (GR/K24079 EPSRC) and a maintenance grant for J.R. We also wish to thank Martin Turnidge for the use of his custom-written software for the collection and analysis of experimental data.

[1] G. J. Wilson, M. L. Turnidge, A. S. Solodukhin, and C. J. S. M. Simpson, Chem. Phys. Lett. **207**, 521 (1993).
[2] M. L. Turnidge, G. J. Wilson, and C. J. S. M. Simpson, Chem. Phys. Lett. **227**, 45 (1994).
[3] J. O. Hirschfelder, C. F. Curtiss, and R. B. Bird, *Molecular Theory of Gases and Liquids* (Wiley, New York, 1954).
[4] J. P. Reid, C. J. S. M. Simpson, and H. M. Quiney, Chem. Phys. Lett. **246**, 562 (1995).
[5] J. P. Reid, C. J. S. M. Simpson, and H. M. Quiney, J. Chem. Phys. **106**, 4931 (1997).
[6] S. Green, J. Chem. Phys. **82**, 4548 (1985).
[7] A. Palma and S. Green, J. Chem. Phys. **85**, 1333 (1986).
[8] A. J. Banks, D. C. Clary, and H. J. Werner, J. Chem. Phys. **84**, 3788 (1986).
[9] J. P. Reid, C. J. S. M. Simpson, and H. M. Quiney, Chem. Phys. Lett. **256**, 531 (1996).
[10] C.-H. Hu and A. J. Thakkar, J. Chem. Phys. **104**, 2541 (1996).
[11] L. Beneventi, P. Casavecchia, G. G. Volpi, C. C. K. Wong, F. R. W. McCourt, G. C. Corey, and D. Lemoine, J. Chem. Phys. **95**, 5827 (1991).
[12] J. J. Andrew, D. C. McDermott, S. P. Mills, and C. J. S. M. Simpson, Chem. Phys. **153**, 247 (1991).

[13] M. L. Turnidge, D. Philos. thesis, Oxford University, 1996.
[14] D. C. Allen and C. J. S. M. Simpson, Chem. Phys. **45**, 203 (1980).
[15] E. T. Chandler, E. A. Gregory, R. M. Siddles, and C. J. S. M. Simpson, Chem. Phys. Lett. **78**, 236 (1981).
[16] M. L. Turnidge, G. J. Wilson, and C. J. S. M. Simpson, Chem. Phys. Lett. **227**, 299 (1994).
[17] M. M. Maricq, E. A. Gregory, C. T. Wickham-Jones, D. J. Cartwright, and C. J. S. M. Simpson, Chem. Phys. **75**, 347 (1983).
[18] C. Douketis, G. Scoles, S. Marchetti, M. Zen, and A. J. Thakkar, J. Chem. Phys. **76**, 3057 (1982).
[19] J. P. Reid, C. J. S. M. Simpson, H. M. Quiney, and J. M. Hutson, J. Chem. Phys. **103**, 2528 (1995).
[20] See, for example, *Atom-Molecule Collision Theory*, edited by R. B. Bernstein (Plenum, New York, 1979), and references therein.
[21] J. M. Hutson and S. Green, MOLSCAT Parallel Computer Code developed from Version 12 (1993) of the serial code by I. J. Bush, distributed by Collaborative Computational Project No. 6 of the EPSRC, UK.
[22] D. E. Manolopoulos and M. H. Alexander, J. Chem. Phys. **86**, 2044 (1987).
[23] J. Bendtsen, J. Raman Spectrosc. **2**, 133 (1974).
[24] R. E. Honig and H. O. Hook, RCA Rev. **21**, 495 (1960).
[25] M. S. Bowers, K. T. Tang, and J. P. Toennies, J. Chem. Phys. **88**, 5465 (1988).
[26] D. A. Micha, Phys. Rev. **162**, 88 (1967).
[27] W. Erlewein, M. von Seggern, and J. P. Toennies, Z. Physik **211**, 35 (1968).
[28] M. von Seggern and J. P. Toennies, Z. Physik **218**, 341 (1969).
[29] G. M. McClelland, K. L. Saenger, J. J. Valentini, and D. R. Herschbach, J. Phys. Chem. **83**, 947 (1979).
[30] J. Tusa, M. Sulkes, and S. A. Rice, J. Chem. Phys. **70**, 3136 (1979).
[31] M. Sulkes, J. Tusa, and S. A. Rice, J. Chem. Phys. **72**, 5733 (1980).
[32] J. Tusa, M. Sulkes, S. A. Rice, and C. Jouvet, J. Chem. Phys. **76**, 3513 (1982).
[33] A. van der Avoird (personal communication).
[34] J. P. Reid, H. M. Quiney, and C. J. S. M. Simpson (unpublished).
[35] G. Ewing, Chem. Phys. **29**, 253 (1978).
[36] W. R. Gentry, J. Chem. Phys. **81**, 5737 (1984).
[37] Y. S. Kim, M. Hutchinson, and T. F. George, J. Chem. Phys. **86**, 5515 (1987).
[38] J. P. Toennies, W. Welz, and G. Wolf, J. Chem. Phys. **71**, 614 (1979).
[39] J. P. Reid, P. W. Barnes, and C. J. S. M. Simpson, Chem. Phys. Lett. **268**, 150 (1997).